Article

Profiling pH Gradients Across Nanocapillary Array Membranes Connecting Microfluidic Channels

Keqing Fa, Joseph J. Tulock, Jonathan V. Sweedler, and Paul W. Bohn

J. Am. Chem. Soc., **2005**, 127 (40), 13928-13933• DOI: 10.1021/ja052708p • Publication Date (Web): 16 September 2005

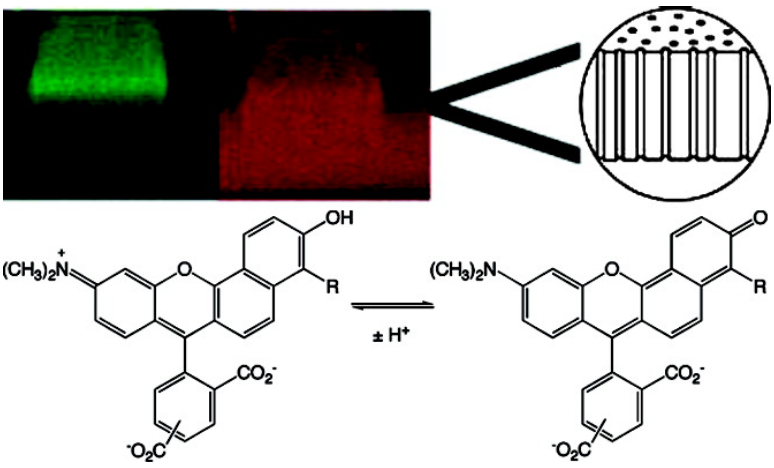

More About This Article

Additional resources and features associated with this article are available within the HTML version:

- Supporting Information
- Links to the 13 articles that cite this article, as of the time of this article download
- Access to high resolution figures
- Links to articles and content related to this article
- Copyright permission to reproduce figures and/or text from this article

View the Full Text HTML

J|A|C|S
ARTICLES
Published on Web 09/16/2005

Profiling pH Gradients Across Nanocapillary Array Membranes Connecting Microfluidic Channels

Keqing Fa, Joseph J. Tulock, Jonathan V. Sweedler, and Paul W. Bohn*

Contribution from the Department of Chemistry and Beckman Institute for Advanced Science and Technology, University of Illinois at Urbana-Champaign, 600 South Mathews Avenue, Urbana, Illinois 61801

Received April 26, 2005; E-mail: bohn@scs.uiuc.edu

Abstract: Nanocapillary array membranes (NCAMs), comprised of thin ($d \sim 5-10\ \mu$m) nuclear track-etched polycarbonate sheets containing $\sim 10^8$ cm^{-2} nearly parallel nanometer-diameter capillaries, may act to gate fluid transport between microfluidic channels to effect, for example, sample collection. There is interest in H^+-transport across these NCAMs because there is significant practical interest in being able to process analyte-containing samples under different pH conditions in adjacent layers of an integrated microfluidic circuit and because protons, with their inherently high mobility, present a challenge in separating microfluidic environments with different properties. To evaluate the capability of NCAMs to support pH gradients, the proton transport properties of NCAMs were studied using laser scanning confocal fluorescence microscopy (LSCFM). Spatiotemporal maps of $[H^+]$ in microfluidic channels adjacent to the NCAMs yield information regarding diffusive and electrokinetic transport of protons. The NCAMs studied here are characterized by a positive zeta potential, $\zeta > 0$, so at small nanocapillary diameters, the overlap of electrical double layers associated with opposite walls of the nanocapillary establish an energy barrier for either diffusion or electrokinetic transport of cations through the nanometer-diameter capillaries due to the positive charge on the nanocapillary surface. Proton transfer through an NCAM into microchannels is reduced for pore diameters, $d \leq 50$ nm and ionic strengths $I \leq 50$ mM, while for large pore diameters or solution ionic strengths, the incomplete overlap of electric double layer allows more facile ionic transfer across the membranes. These results establish the operating conditions for the development of multilevel integrated nanofluidic/microfluidic architectures which can support multidimensional chemical analysis of mass-limited samples requiring sequential operations to be implemented at different pH values.

Introduction

Research exploring micro total analysis systems (μ-TAS) has grown exponentially over the past few years. Microfluidically actuated μ-TAS techniques have been demonstrated to be applicable to many different kinds of assays and analytical operations,[1−5] particularly those involving the detection and characterization of biomolecule-containing samples. By combining sequentially linked operations, such as separation/detection/measurement into a single device via miniaturization, significant improvements in speed, selectivity, and detection limit can be realized compared to conventional bench-scale procedures.

Hybrid nanofluidic/microfluidic architectures for rapid sample preparation, separation, transport, and detection are being pursued in a number of laboratories.[6−14] Capillary array membranes containing 10−200 nm diameter cylindrical pores are employed as interconnects to establish controllable fluidic communication between micrometer-scale channels operating in vertically separated planes. The microfluidic channels are constructed either in poly(dimethylsiloxane) (PDMS) or poly(methyl methacrylate) (PMMA), and the nanocapillary array membranes (NCAMs) are made of track-etched polycarbonate (PCTE) with a poly(vinylpyrrolidone) coating. The key feature of nanofluidic transport is that fluid flow occurs in structures with diameters, d, of the order of the Debye length,

(1) Jiang, X.; Jessamine, M. K. Ng; Stroock, A. D.; Dertinger, S. K. W.; Whitesides, G. M. *J. Am. Chem. Soc.* **2003**, *125*, 5294.
(2) Peterson, D. S. *Lab on a Chip* **2005**, *5*, 132.
(3) Liu, J.; Pan, T.; Woolley, A. T.; Lee, M. L. *Anal. Chem.* **2004**, *76*, 6948.
(4) Gao, J.; Xu, J.; Locascio, L. E.; Lee, C. S. *Anal. Chem.* **2001**, *73*, 2648.
(5) Dai, J.; Ito, Takashi; Sun, L.; Crooks, R. M. *J. Am. Chem. Soc.* **2003**, *125*, 13026.
(6) Kuo, T. C.; Cannon, D. M., Jr.; Shannon, M. A.; Bohn, P. W.; Sweedler, J. V. *Sens. Actuators, A* **2003**, *102*, 223.
(7) Kuo, T. C.; Cannon, D. M., Jr.; Chen, Y. N.; Tulock, J. J.; Shannon, M. A.; Sweedler, J. V.; Bohn, P. W. *Anal. Chem.* **2003**, *75*, 1861.
(8) Cannon, D. M., Jr.; Kuo, T. C.; Bohn, P. W.; Sweedler, J. V. *Anal. Chem.* **2003**, *75*, 2224.
(9) Kuo, T. C.; Kim, H. K.; Cannon, D. M., Jr.; Shannon, M. A.; Sweedler, J. V.; Bohn, P. W. *Angew. Chem., Int. Ed.* **2004**, *43*, 1862.
(10) Kuo, T. C.; Sloan, L. A.; Sweedler, J. V.; Bohn, P. W. *Langmuir* **2001**, *17*, 6298.
(11) Daiguji, H.; Yang, P. D.; Majumdar, A. *Nano Lett.* **2004**, *4*, 137−142.
(12) Foote, R. S.; Khandurina, J.; Jacobson, S. C.; Ramsey, J. M. *Anal. Chem.* **2005**, *77*, 57−63.
(13) O'Brien, M. J.; Bisong, P.; Ista, L. K.; Rabinovich, E. M.; Garcia, A. L.; Sibbett, S. S.; Lopez, G. P.; Brueck, S. R. J. *J. Vac. Sci. Technol. B* **2003**, *21*, 2941−2945.
(14) Pu, Q. S.; Yun, J. S.; Temkin, H.; Liu, S. R. *Nano Lett.* **2004**, *4*, 1099−1103.

10.1021/ja052708p CCC: $30.25

κ^{-1}. Thus, fluid motion can occur in one of two limiting regimes characterized by the dimensionless product, κd. When $\kappa d \gg 1$, the large diameter limit applies, and flow is dominated by ion migration. In contrast, when $\kappa d \leq 1$, co-ions are repelled from the interior of the nanopore, and flow is dominated by counterion motion. Since κ depends directly on the ionic strength and the physical extent of the electrical double layer, the movement of fluids across the NCAM in this architecture is driven and precisely controlled by the external electrical bias. The NCAM can, thus, act as a controllable fluidic switch, leading to applications as a microreactor and in fast chemical mixing.[9]

A fully controllable gate is characterized by fluidic isolation in the "off" state and tunable fluidic transport in the "on" state. Furthermore, just understanding the volume flow rate is insufficient for a full description of nanofluidic flow because different ions exhibit differential transport rates in nanometer-diameter capillaries,[15] leading to selective transport in electrokinetic flow across NCAMs. For example, transient variation of the electrical current, as measured in the receiving or the source microchannel, upon application of a forward bias potential to an NCAM yields behavior which is, in general, much more complicated than one might be led to expect based on a simple equivalent circuit model. It is critical to understand the nature of differential transport of ions and molecules in nanoscale confined structures because of their importance for the development of bio-NEMS (Nano-Electro-Mechanical-Systems) and μ-TAS applications.[16−26] In this regard, the surface charge density, σ, nanopore diameter, ionic strength of the transporting solution, I, and the mass/charge ratio and the inherent mobility of solution constituents are key factors in determining the observed transport behavior.

One of the goals of the NCAM architecture is controlled isolation of solutions of different composition and the ability to process analyte-containing samples under different conditions in adjacent layers of an integrated microfluidic circuit. The pH plays a central role in these design considerations. For example, frequently, a separation of a complex mixture is best carried out under acidic conditions, but the fluorescent detection of the labeled analytes is optimized under basic conditions. As another example, the common electrolytes used in electrophoretic separations often contain additives that decrease the performance of electrospray mass spectrometry by orders of magnitude. The ability to optimize an electrophoretic separation in a microfluidic device and then transfer mass-limited separated analyte bands from one fluidic environment into another before introducing them to the detection system, whether fluorescence or mass spectrometry, greatly increases overall system performance and allows each "module" of the multidimensional determination to be optimized separately.

Table 1. Membrane Properties

pore size (nm)	pore density (cm^{-2})	average spacing between pores (μm)	number of pores for a 50×50 μm^2 area
10	6×10^8	0.41	1.5×10^4
50	6×10^8	0.41	1.5×10^4
200	3×10^8	0.58	7.5×10^3

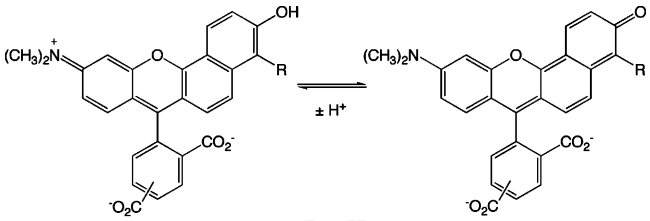

1: R = H;
2: R = F

A critical question involves how well NCAMs effect ionic isolation. We probe the H^+-transport across NCAMs because protons, with their inherently high mobility in aqueous media, present the most extensive challenge to preparing microfluidic environments with different properties. A further advantage is that pH gradients across NCAMs can be precisely monitored using fluorescent probes, such as carboxyseminaphthorhodafluor, **1**, in combination with laser scanning confocal microscopy (LSCM). The dye **1** absorbs light at the absorption peak of 488 nm and exhibits a shift in fluorescence emission from 588 nm in the acidic form to 640 nm in the basic form.[27] The characterization of pH gradients and ionic transport, by spatiotemporal profiling of $[H^+]$ with and without external bias, provides information critical to the performance of NCAMs in hybrid nanofluidic/microfluidic structures for multidimensional, multilevel chemical characterization of complex samples.

Experimental Section

Materials. Nanoporous polycarbonate track-etched membranes were purchased from Osmonics (Minnetonka, MN) and stored under dry N_2 prior to use. These membranes have highly monodisperse distributions of pore diameters, with pore densities ranging from 3×10^8 to 6×10^8 cm^{-2}. Table 1 shows selected properties of these membranes.

Dye **1** (Molecular Probes, Eugene, OR) was used as the fluorescent pH indicator. All solutions of **1** were prepared to a concentration of 16.96 μM in 18 MΩ cm deionized (DI) water. A series of stock 50 mM phosphate (Sigma-Aldrich, Milwaukee, WI) buffer solutions (PBS) from pH 4.5 to 9.5 were prepared in DI water.

Fabrication of the μ-TAS Devices. Standard rapid prototyping protocols and soft lithography processes were used to fabricate PDMS layers with embedded microchannel geometries and reservoirs.[28,29] First, a negative design mask was printed on a transparency (5080 dpi, Printing Services, University of Illinois at Urbana-Champaign). This transparency served as the photomask in photolithography to produce a positive relief feature on silicon (Silicon Quest International, Santa Clara, CA) using SU 8-2050 photoresist (Microlithography Chemical Corp., Newton, MA). Prepolymer Sylgard 184 and curing agent (Dow Corning Corp., Midland, MI) were thoroughly mixed in a 10:1 w:w

(15) Chaterjee, A.; Cannon, D. M., Jr.; Gatimu, E. N.; Aluru, N.; Sweedler, J. V.; Bohn, P. W. *J. Nanopart. Res.*, in press.
(16) Loughnane, B. J.; Farrer, R. A.; Scodinu, A.; Reilly, T.; Fourkas, J. T. *J. Phys. Chem. B* **2000**, *104*, 5421.
(17) Cheng, J. T.; Giordano, N. *Phys. Rev. E* **2002**, *65*, 031206.
(18) Qiao, R.; Aluru, N. R. *J. Chem. Phys.* **2003**, *118*, 4692.
(19) Pu, Q. S.; Yun, J. S.; Temkin, H.; Liu, S. R. *Nano Lett.* **2004**, *4*, 1099.
(20) Daijuji, H.; Yang, P. D.; Majumdar, A. *Nano Lett.* **2004**, *4*, 137.
(21) Travis, K. P.; Gubbins, K. E. *J. Chem. Phys.* **2000**, *112*, 1984.
(22) Thompson, A. P. *J. Chem. Phys.* **2003**, *119*, 7503.
(23) Karlsson, R.; Karlsson, M.; Karlsson, A.; Cans, A. S.; Bergenholtz, J.; Akerman, B.; Ewing, M.; Voinova, A. G.; Orwar, O. *Langmuir* **2002**, *18*, 4186.
(24) Stein, D.; Kruithof, M.; Dekker, C. *Phys. Rev. Lett.* **2004**, *96*, 035901.
(25) Han, J.; Turner, S. W.; Craighead, H. G. *Phys. Rev. Lett.* **1999**, *83*, 1688.
(26) Kemery, P. J.; Steehler, J. K.; Bohn, P. W. *Langmuir* **1998**, *14*, 2884.
(27) Molecular Probes Handbook: Eugene, OR.
(28) McDonald, J. C.; Duffy, D. C.; Anderson, J. R.; Chiu, D. T.; Wu, H. K.; Schueller, O. J. A.; Whitesides, G. M. *Electrophoresis* **2000**, *21*, 27.
(29) Duffy, D. C.; McDonald, J. C.; Schueller, O. J. A.; Whitesides, G. M. *Anal. Chem.* **1998**, *70*, 4974.

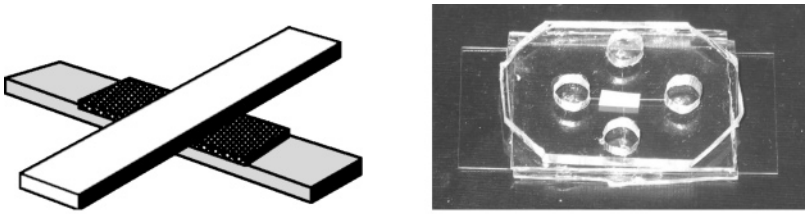

(a) (b)

Figure 1. (a) Schematic diagram of a three-dimensional gated injection separation device consisting of two crossed microfluidic channels with an NCAM interconnect. (b) Photograph of the fabricated hybrid nanofluidic/microfluidic device. The white structure in the center of the device is the PCTE membrane with 200 nm pores.

ratio. The mixture was poured onto the fully developed silicon master and cured for ~18 h at room temperature. A partial curing technique was developed to achieve optimum sealing of the PDMS around the PCTE membrane. When the polymer mixture had reached the proper curing time, but prior to being completely cured, the sticky PDMS layers were peeled from the silicon master, while maintaining the shape of the microchannels, and the PDMS microchannel/PCTE nanochannel/PDMS microchannel structures were assembled. Care was taken while trimming the PCTE membranes and assembling the sandwich structures to prevent any damage to the membranes. The hybrid nanofluidic/microfluidic device was designed with a junction area of $50 \times 50\ \mu m^2$ in the center of the device, where the two 2 cm long $50 \times 50\ \mu m^2$ cross-section microchannels intersect (Figure 1).

Procedures. Microchannels were filled with solutions by vacuum. Fluorescence images were collected using a laser scanning confocal fluorescence microscope (Model TCS SP2, Leica Microsystems, Inc.). Whenever electrokinetic flow was required, platinum wires (250 μm diameter, Goodfellow Corp., Berwyn, PA) were placed into the reservoirs to provide electrical bias. A Labview (National Instruments Corp., Austin, TX)-based computer-controlled eight-relay system was used to switch the high voltage power supply (Bertan High Voltage, Hicksville, NY, 0−3 kV) and supply electrokinetic transport bias voltages. The filling of the microchannel was tested by measuring the current across the channel. The nanocapillary interconnect array was conditioned for at least 5 min at low bias (15 V) before electrokinetic transport experiments across the PCTE membrane and the microchannel.

An Ar^+ laser ($P \sim 3$ mW) was used for excitation at 488 nm. The laser was focused into the junction region by a 10× air-immersion objective after reflecting off a dichroic mirror. Scattered light and out-of-focus fluorescence were blocked by a ~64 μm pinhole. Fluorescence images were collected at a resolution of 512 × 512 pixels in the XZT or XZY mode at two wavelengths: 588 and 640 nm. Two photomultiplier tube detectors were tuned and set to have equal response for both wavelengths.

In XZT mode, images were acquired at a single $x-z$ plane in the center of the microchannel junction as a function of time to determine the pH profile for time-varying conditions. In XZY mode, used for characterization of stationary solutions, $x-z$ fluorescence images were acquired at different spatial (y) positions along the junction region and averaged to minimize variations due to image position. It was found, however, that the ratio of fluorescent intensities did not vary significantly with position at constant pH. Image processing was accomplished with image analysis software, ImageJ (freeware), and was used to calculate the ratio of spatially averaged fluorescent intensities in the region of interest for images at the two emission wavelengths.

Results and Discussion

Spatial pH Measurements. Both dye molecules (**1** and **2**, see Supporting Information) have two pH-dependent emission peaks in the fluorescence spectrum centered at 588 and 640 nm when excited between 488 and 530 nm.[27] The dye **1** has a pK_a of ~7.5 and, consequently, a useful range of pH 6−9. In contrast, the fluorinated derivative **2** exhibits a transition at lower pH since **2** has a p$K_a \sim 6.4$. Quantitatively measuring the intensity ratio of the dual emission peaks at a given spatial location enables the accurate determination of pH at that location using the equations shown in the Supporting Information. As shown in the calibration plots in the Supporting Information, we obtain excellent linear ($r^2 > 0.99$) correlation between optical and potentiometric pH values, demonstrating that accurate values of pH can be determined from fluorescence images in these structures.

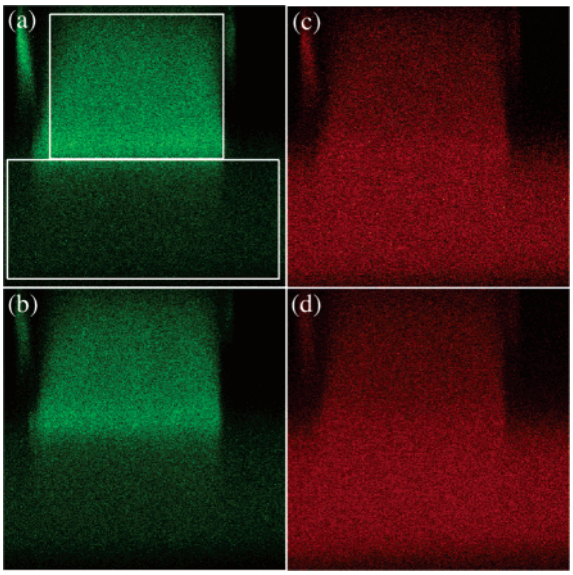

Figure 2. XZT fluorescent images (false color) showing the spatial pH profile as a function of time across a 10 nm membrane with an initial pH offset of ΔpH = 3.06 and no flow. Image sections are perpendicular to the long axis of the upper channel and parallel to the long axis of the lower channel. (a) $\lambda_{em} = 588$ nm, $t = 2$ min; (b) $\lambda_{em} = 588$ nm, $t = 120$ min; (c) $\lambda_{em} = 640$ nm, $t = 2$ min; (d) $\lambda_{em} = 640$ nm, $t = 120$ min. The approximate positions of the upper and lower microchannels are shown by the white rectangles in panel (a). After 120 min, the pH offset is maintained, as indicated by the fact that the fluorescence intensity contrasts of the upper channel and lower channels are unaltered.

pH Gradients Across NCAMs in Static Solutions. A basic question concerns the ability of NCAMs to segregate two solutions at different pH values when there is no flow in either microchannel. To probe this question, a structure was prepared in which the upper microchannel was filled with buffer solution at pH 4.62, while the initial pH of the buffer solution in the lower microchannel was 7.68, establishing an initial pH gradient, ΔpH = 3.06 across the hydrophilic PCTE membrane. The fluorescent images in Figure 2 show $x-z$ slices through the center of the vertically stacked, crossed microchannels. Visually, the upper channel shows greater intensity at $\lambda_{em} = 588$ nm (viz.

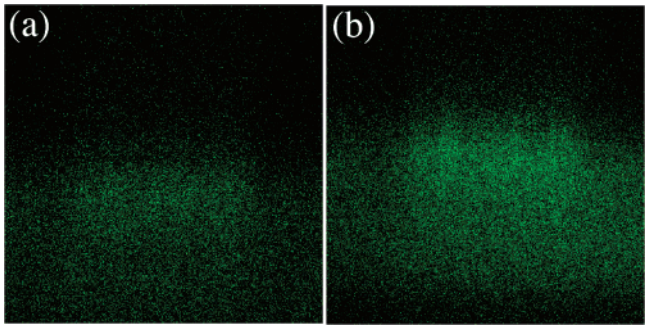

Figure 3. XZT fluorescent images (false color) showing the spatial pH profile as a function of time across a 200 nm membrane with an initial pH offset of ΔpH = 3.06 and no flow. (a) λ_{em} = 588 nm, t = 2 min; (b) λ_{em} = 588 nm, t = 60 min. Note: 200 nm PCTE membranes are highly scattering (opaque), cf. Figure 1b, so only the lower microchannel is visible. The increased fluorescence intensity in (b) results from proton leakage from the upper to the lower microchannel across the 200 nm NCAM. Consistent with this interpretation, the fluorescence intensity at 640 nm (not shown) decreases after 60 min.

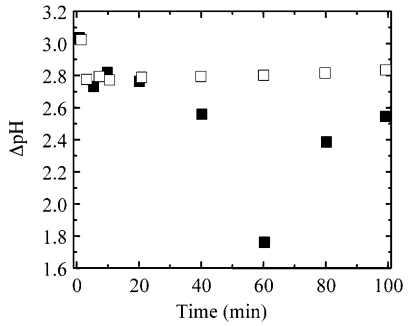

Figure 4. Comparison of the pH offset between upper and lower microchannels as a function of time for structures separated by 10 nm (□) and 200 nm (■) pore diameter NCAMs.

Figure 2a,b), the wavelength of maximum emission of the acidic form of **1**, and the lower channel shows stronger emission at 640 nm (viz. Figure 2c,d), the wavelength of maximum emission of the basic form of **1**. The striking feature of these images is that it is clear that the pH difference is sustained, even after 2 h. Similar behavior was observed for a structure employing a 50 nm pore diameter NCAM (data not shown). Figure 3 illustrates the behavior of a similar structure with a 200 nm pore diameter NCAM. Visually, the intensity of 588 nm emission in the lower microchannel significantly increases in the first 60 min, consistent with quantitative pH measurements using eqs S1 and S2 in the Supporting Information, which establish that the initial ΔpH = 3.06 drops to ΔpH = 1.76 at 60 min.

The temporal behavior of the pH offset for both 10 and 200 nm pore diameter NCAMs is shown in Figure 4. The structure with a 10 nm pore diameter membrane exhibits an initial pH drop of ca. 0.2, but then maintains a steady ΔpH for the remainder of the experiment. The highly scattering nature of the 200 nm pore diameter NCAMs yields measurements with larger uncertainties. Nevertheless, a decrease in the pH offset of ~1.3 was observed for the 200 nm membrane at 60 min, and the long-time pH offset for the 200 nm NCAM structure is clearly larger than that for the 10 nm NCAM structure. Table 2 summarizes the results of quantitative pH offset experiments in the absence of electrokinetic flow in the microchannels. Because some of the resistance to pH change evident in the images of Figure 2 and the data in Table 2 could potentially be attributed to the buffering action of the PBS in the lower microchannel, experiments were performed in the absence of buffer, also. The results are summarized on the right side of Table 2. Although the change in pH offset, $\Delta(\Delta\text{pH}) = \Delta\text{pH}(t) - \Delta\text{pH}(0)$, is larger than the value for the buffered solutions, the general trends in the data are the same in both cases. In general, it is clear that significant pH offsets across the hydrophilic NCAMs are sustained for hours for the 10 and 50 nm membranes, while significant proton leakage occurs in structures employing NCAMs with larger pore sizes, such as the 200 nm pore diameter NCAM investigated here. Strikingly, the 200 nm pore diameter structure in the absence of buffering shows complete equilibration, that is, all of the initial pH offset disappears under these conditions, $\Delta(\Delta\text{pH}) = \Delta\text{pH}(0)$, further highlighting the significance of the small and constant pH drops seen for the smaller pore diameter NCAMs.

NCAM pH Gradients in the Presence of Electrokinetic Flow in the Microchannels. The NCAM molecular gate is the enabling component for construction of integrated three-dimensional microfluidic architectures mediating preparation, transport, separation, and detection of mass-limited samples for multidimensional chemical analysis. Previous work in this laboratory has shown that fluid injection across NCAMs can be precisely controlled by tuning the magnitude and duration of the external bias pulse.[6] Ideally, NCAM molecular gates selectively and rapidly transport fluids from the source channel to the receiving channel for further processing when the gate is forward-biased (on), while fluidic communication between the two microchannels is completely isolated when the gate is reverse-biased (off). The data presented above, in the absence of electrokinetic flow in the microchannel, illustrate that, in the off state, the positively charged NCAM membranes with pore diameters, $d \leq 50$ nm, substantially isolate the cationic content of the two microchannels, even for highly mobile species, such as H^+.

Figure 5 shows the behavior of the pH gradient across 10 and 50 nm pore diameter membranes when electrokinetic flow is maintained in both microchannels. In situations like the one shown in Figure 5, in which flow is maintained in one or both microchannels, the question of bias across the NCAM must be answered by network analysis of the four-terminal device (inset, cf. Figure 6 of ref 6). Denoting the potentials applied to the two source (receiver) microchannel arms as $V_{S(1,2)}$($V_{R(1,2)}$), the impedances in the respective microchannel arms as $R_{S(1,2)}$($R_{R(1,2)}$) and the membrane impedance as R_M, the bias across the NCAM, $\Delta V = V_{MS} - V_{MR}$, can be obtained from straightforward network analysis by solving the simultaneous equations:

$$\frac{V_{S1} - V_{MS}}{R_{S1}} = \frac{V_{MS} - V_{S2}}{R_{S2}} + \frac{V_{MS} - V_{MR}}{R_M}$$

$$\frac{V_{MR} - V_{R2}}{R_{R2}} = \frac{V_{R1} - V_{MR}}{R_{R1}} + \frac{V_{MS} - V_{MR}}{R_M}$$

In practice, one always knows the voltages $V_{S(1,2)}$($V_{R(1,2)}$) and the total microchannel impedances, $R_S = R_{S1} + R_{S2}$ and $R_R = R_{R1} + R_{R2}$. Reasonable estimates of the individual microchannel arm impedances can most easily be made by careful balancing, such that $R_{S1} = R_{S2}$ and $R_{R1} = R_{R2}$.

Under the conditions of the experiment shown in Figure 5, we estimate that $V_{MS} > V_{MR}$. Since the NCAM has a positive

Table 2. Summary of ΔpH Behavior for Various NCAMs and Initial pH offsets

pore diameter (nm)	ΔpH change lower channel buffered with PBS			ΔpH change lower channel unbuffered		
10	0.08, (2.0)[a]	0.18, (3.0)	0.23, (4.0)	0.38, (2.0)	0.41, (3.1)	0.29, (3.6)
50	0.10, (2.0)	0.16, (3.0)	0.39, (4.0)	0.34, (2.6)	0.33, (3.0)	0.48, (3.3)
200		1.28, (3.0)			3.00, (3.0)	

[a] Table entries are given as pairs Δ(ΔpH), (ΔpH(t=0)). Data are average values of three repeated experiments.

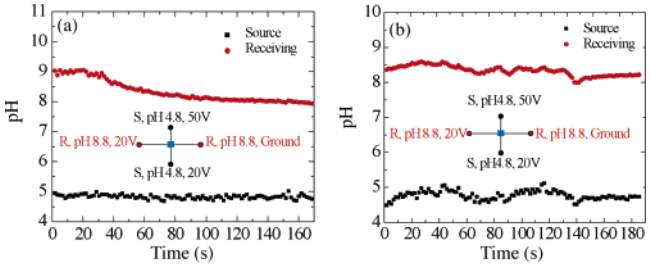

Figure 5. Temporal behavior of pH gradients across (a) 10 nm and (b) 50 nm pore diameter NCAMs in the presence of electrokinetic flow. The bias configuration is shown in the inset of each panel. S(R) denotes the source (receiver) channel, and the ionic strength was maintained at 50 mM in both channels.

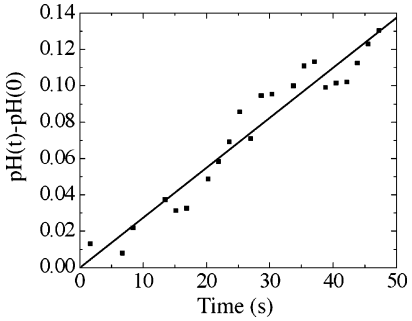

Figure 6. Plot of the initial change in pH in the receiving channel as a function of time using the 10 nm pore diameter NCAM.

zeta potential, $\zeta > 0$, the counterions are anions, and since the NCAMs studied in Figure 5 are small diameter ($\kappa d \sim 1$), transport should be dominated by counterion motion, that is, the co-ion population ~ 0. The network analysis indicates that the receiving side of the NCAM is negative relative to the source side, meaning that any anion-dominated fluid transport should be from receiving to source side, that is, in the direction opposite that obtained under forward-bias conditions. However, it follows that it is also forward-biased with respect to the transport of H^+, which are co-ions under these conditions. Furthermore, the zeta potentials of the walls of the microchannels (PDMS) and the interior surfaces of the nanocapillaries (poly(vinylpyrrolidone)-coated polycarbonate) are of opposite polarities.[30,31] As noted in an earlier study,[6] the direction of forward-bias under these conditions is determined by the magnitude of the membrane potential, ΔV, with smaller NCAM pore diameters leading to larger ΔV values and control of the overall flow direction by the polarity of the nanochannels. Although the bias across the NCAM favors ion migration of H^+, it is evident that a pH gradient, $\Delta pH \sim 3.5$ for the initial $\Delta pH(0) = 4.0$, is maintained across the 10 nm pore diameter NCAM under the conditions of Figure 5. This reflects the strong overlap of the electrical double layers associated with opposite walls of the NCAM nanochannels when $\kappa d \leq 1$ and the concomitant exclusion of cations from the nanocapillaries. Figure 5b shows that the behavior of the pH gradient across the 50 nm pore diameter membrane is similar than that across the 10 nm membrane when similar electrokinetic microfluidic flow conditions are maintained. Simply applying the same bias voltages, $V_{S(1,2)}(V_{R(1,2)})$, does not produce the same membrane potential because the membrane impedance, which depends on the number and diameter of the pores, is different in the two cases. Nevertheless, a pH gradient of $\Delta pH = 3.5$ is stable under microchannel flow conditions for more than 3 min, as shown in Figure 5b.

Transport Rate Comparison. To better understand how surface charges on the interior of the nanopores control selective ion transport under potential control, it is desirable to compare the observed H^+-transport rates with that expected from simple diffusion across the NCAM. Assuming that the proton transport across the NCAM is a first-order kinetic process with rate constant k_1, the initial change in pH can be expressed as

$$pH = pH_0 + \left(k_1 - \frac{k_2}{K_a}[A^-]\right) t$$

where $[A^-]$ is the concentration of the basic form of the dye **1** in the receiving microchannel, k_2 is the (forward) rate constant for the protonation reaction of **1**, and K_a is the acid dissociation constant. In this region, the change in concentration of either the acidic or basic form of **1** is very small, so $[A^-]$ can be considered to be approximately constant. Shown in Figure 6 is the initial rate of change of pH resulting from proton transfer from the source channel to the receiving channel with a transport rate of k

$$k = k_1 - \frac{k_2}{K_a}[A^-]$$

The slope in Figure 6 gives a proton transport rate of $k = 0.0028\ s^{-1}$, giving a characteristic time, $t = 1/k \approx 356$ s, for proton transport through the NCAM. The membrane used in the experiment shown in Figure 6 is $\sim 6\ \mu$m thick. If the proton diffusion coefficient at 298 K is $D_H = 9.31 \times 10^{-9}\ m^2/s$,[32] the time for a proton to diffuse across the nanocapillary can be estimated as $t_{diff} \sim \langle x \rangle^2/D \approx 3.9 \times 10^{-3}$ s $= 3.9$ ms, which is ca. 5 orders of magnitude faster than the characteristic proton transport rate measured in Figure 6. Although the comparison is almost certainly not quantitatively accurate, it is reasonable to conclude from this calculation that the barrier established by the nanopore substantially reduces the transport rate of (positively charged) protons. Thus, molecular gates constructed from NCAMs exploit the nanopore surface charge characteristics to

(30) Liu, Y.; Fanguy, J. C.; Bledsoe, J. M.; Henry, C. S. *Anal. Chem.* **2000**, *72*, 5939.
(31) Ren, X. Q.; Bachman, M.; Sims, C.; Li, G. P.; Allbritton, N. *J. Chromatogr. B* **2001**, *762*, 117.
(32) Atkins, P. *Physical Chemistry*, 6th ed.; Freeman: New York, 1999; p 749.

selectively screen ions and, for the polarities chosen, to provide a barrier to proton leakage under conditions supporting active electrokinetic flow in the microchannels. Of course, when NCAMs with large pore diameters are used, the barrier is substantially reduced, and it is possible for the positively charged proton to transit the nanocapillaries, thereby equilibrating the pH on either side of the NCAM.

Conclusions

The performance of NCAM-based molecular gates in isolating vertically separated microchannels under both static and microfluidic flow conditions was examined by profiling the pH offsets across the NCAM. In both cases, substantial pH offsets are sustained by the NCAM when membrane pore diameters are $\leq$50 nm. The surface charge of the interior of the NCAM nanocapillaries mediates selective ion transport due, mainly, to two effects: the positive ζ-potential and the overlap of the electrical double layer when $\kappa d \leq 1$. Thus, at small pore diameters in the absence of a specific forward-bias across the NCAM, cations are excluded, while anions are allowed to move freely in the interior of the nanocapillaries. We note, finally, that all of the observations here are consistent with, and complementary to, the recent work by Korzeniewski and coworkers who derivatized nanochannels with $-SO_3H$ moieties to produce $\zeta < 0$ surfaces in which cations, primarily H^+, were the enhanced population counterions.[33] In these structures, the enhanced H^+ populations led to enhanced proton conductance.

These observations have important implications for the use of NCAM-based fluidic switching elements in multilayer, multidimensional chemical analysis platforms, inasmuch as it is often desirable to carry out one manipulation at a certain pH and ionic strength and a subsequent manipulation at substantially different solution conditions. This work shows that the interplay of pore size, surface charge density, analyte charge, and solution ionic strength allow control over undesirable "leakage" across the NCAM either without or with electrokinetic flow in the surrounding microchannels. The gate performance is expected to provide the desirable control over the molecular separation, transport, and injection in the development of multidimensional and multilayer structure.

Acknowledgment. This work was supported by the National Science Foundation under Grant DMI-0329162, the Department of Energy under DE FG02 88ER13949, and the National Institutes of Health under DA018310.

Supporting Information Available: Determination of pH and calibration of pH measurements. This material is available free of charge via the Internet at http://pubs.acs.org.

JA052708P

(33) Liu, S.; Pu, Q.; Gao, L.; Korzeniewski, C.; Matzke, C. *Nano Lett.* **2005**, ASAP.